Nonlinear optical responses in multiorbital topological superconductors

Arpit Raj,[1,*] Abigail Postlewaite,[1] Swati Chaudhary,[2,1,3] and Gregory A. Fiete[1,3]
[1]*Department of Physics, Northeastern University, Boston, Massachusetts 02115, USA*
[2]*Department of Physics, The University of Texas at Austin, Austin, Texas 78712, USA*
[3]*Department of Physics, Massachusetts Institute of Technology, Cambridge, Massachusetts 02139, USA*

(Received 4 January 2024; accepted 3 May 2024; published 13 May 2024)

We theoretically study first- and second-order optical responses in a transition-metal dichalcogenide monolayer with distinct trivial, nodal, and time-reversal invariant topological superconducting (TRITOPS) phases. We show that the second-order dc response, also known as the photogalvanic response, contains signatures for differentiating these phases while the first-order optical response does not. We find that the high-frequency photogalvanic response is insensitive to the phase of the system, while the low-frequency response exhibits features distinguishing the three phases. At zero doping, corresponding to an electron filling in which the Fermi level lies at nodal points, there are opposite sign zero-frequency divergences in the response when approaching the nodal phase boundaries from the trivial and the TRITOPS phases. In the trivial phase, both the high-frequency and low-frequency response of the system are negative, but in the TRITOPS phase the low-frequency response becomes positive while the high-frequency response remains negative. Furthermore, since phase transitions are controlled by the Rashba spin-orbit coupling and the ratio of intraorbital and interorbital paring amplitudes, our results not only help distinguish the phases but they can also provide an estimate of the pairing amplitudes based on the photogalvanic response of the system.

DOI: 10.1103/PhysRevB.109.184514

I. INTRODUCTION

The second-order nonlinear optical response serves as a highly effective tool for probing symmetry-broken states [1,2]. The second-order dc response to an alternating electric field, also known as the photogalvanic effect, has taken central stage recently [3–17]. Photogalvanic effects have been widely employed for probing the symmetries of quantum phases, as well as nontrivial quantum geometries of electronic bands [18–29]. Recent theoretical works have established that nonlinear responses are interesting for noncentrosymmetric superconductors [30–33] and can aid in the characterization of the phase (topological or trivial) and order-parameter symmetry of experimentally identified superconductors.

While the linear optical conductivity has long been used to probe quantities like spectral weight transfer, the nature of the superconducting state, and the magnitude of the superconducting gap [34–37], recent experiments have also studied nonlinear optical properties of cuprate superconductors, revealing the nature of the broken symmetries in the pseudogap phase [38]. It was proposed in Ref. [30] that the signatures of inversion-breaking superconductivity are much stronger in second-order optical effects than in the linear optical conductivity, and they can persist over a relatively wide range of temperatures, making the nonlinear response an important quantity to study.

The absence of inversion symmetry in noncentrosymmetric superconductors allows for the coexistence of opposite parity pairing channels leading to a mixed-parity order parameter [39–45]. A mixed-parity order parameter can lead to the emergence of exotic superconducting effects, such as the nonreciprocal Meissner effect [46], finite momentum pairing states [47,48], topological superconductivity [49,50], and helical superconductivity [51]. Monolayer and few-layer transition-metal dichalcogenides (TMDs) are known for their wealth of electronic and magnetic phases [52–54]. At low temperatures, TMDs constitute one class of superconductors that have been identified as highly suitable candidates for a mixed-parity pairing potential and exotic superconductivity [55–59].

Layered TMDs are proving to be a highly versatile platform for studying unconventional superconductivity [60–65]. TMD monolayers MX_2 (M = Mo, W, Nb, Ta; X = S, Se, Te) lack an inversion center and have significant electronic correlations and spin-orbit coupling (SOC), which makes them ideal candidates for topological superconductivity and unconventional pairing [60,65,66]. The unconventional superconductivity in group VI TMDs is usually induced by external factors like ionic gating, doping, and intercalation [47,54,56,65,67,68], with the exception of $2M$-WS_2, which is an intrinsic topological superconductor [67]. Group VI layered TMDs $NbSe_2$ and TaS_2 are known for naturally occurring Ising superconductivity [69–77], which shows remarkable stability to in-plane magnetic fields.

Group VI layered TMDs have gained significant attention as they can exhibit many exotic superconducting features, such as nodal superconductivity [78], collective Leggett modes [79], and topological boundary modes [63]. In addition to Ising SOC, the multiband and mixed-parity nature of the

*raj.a@northeastern.edu

pairing terms [80–82] also endows the superconductivity with many intriguing features in these materials. All these factors lead to a rich phase diagram where superconducting phases with different topological features can be obtained by tuning the in-plane magnetic field, Rashba SOC, and interorbital pairing term [82–86]. Thus, this class of TMDs is important for the investigation of topological superconductivity. It is crucial to characterize the different phases that can be obtained in this class of superconductors and predict what their signatures will be in different types of measurements. Given the controversy around claims of topological superconductivity, it is important to correlate measurements of different types, each of which can provide evidence either for or against topological superconductivity.

Atomically thin TaS_2 has recently emerged as a compelling candidate with significant potential for the realization of topological superconductivity [73,87,88]. Ising superconductivity in this material can be enhanced through electron doping or by reducing the number of atomic layers [88], a phenomenon often ascribed to the suppression of a charge-density wave [73]. Possible signatures of topological superconductivity have been observed in 2H-TaS_2, which displays a zero-bias conductance peak in detached flakes of superconducting samples [87], and most recently in 4Hb-TaS_2 (which consists of alternately stacked 1H-TaS_2 and 1T-TaS_2) which hosts one-dimensional boundary modes [63]. The interorbital pairing channel is crucial for nontrivial topology in layered TaS_2, and by changing the strength of the interorbital pairing term in 1H-TaS_2, the system can be driven from a conventional superconductor to a nodal superconductor, and then to a fully gapped time-reversal invariant topological superconductor (TRITOPS) [82].

In this work, we explore the possibility of using the nonlinear optical response (NLOR) to distinguish different topological phases in 1H-TaS_2. We study the first- (for a linear response comparison) and second-order dc conductivity in three different phases: (i) trivial, (ii) nodal, and (iii) TRITOPS. In 1H-TaS_2, the topological features of the superconducting phase are determined by the Rashba SOC and the ratio of on-site intraorbital and interorbital superconducting pairing terms [82], which have opposite parity. It has been shown that photocurrents can carry strong signatures of mixed-parity and multiband pairing terms [32,33,36]. Multiband systems also allow for some intrinsic optical excitations which are absent in single-band models [36] and hence may manifest strongly in nonlinear optical responses as well. The multiorbital nature of superconductivity pairing also leads to nontrivial quantum geometry engendering features like flat-band superconductivity [89–95]. Similar quantum geometric aspects also lead to unique signatures in light-matter coupling based processes [96] and in particular manifest very strongly in nonlinear optical responses [2–4,20,23].

Motivated by these works, we calculate the second-order dc response of 1H-TaS_2 for linearly polarized light. We find that the low-frequency behavior exhibits distinguishing features for three superconducting phases and can serve as a reliable probe to characterize the nature of a superconducting state in this exciting Ising superconductor. A schematic for the distinct types of second-order response and the associated superconducting phases is shown in Fig. 1.

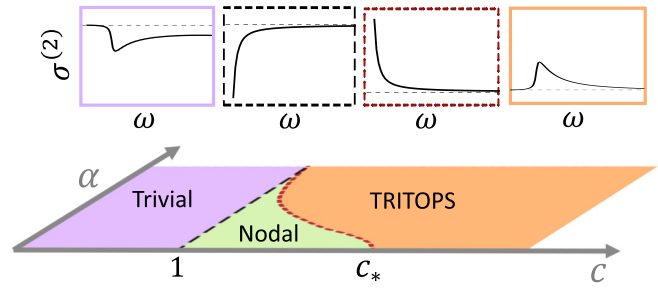

FIG. 1. Schematic representation of second-order conductivity in different superconducting phases of 4Hb-TaS_2 for low frequencies (close to the superconducting pairing strength). The two gapped phases—shown in purple (trivial) and orange (TRITOPS)—have the opposite sign of the second-order conductivity. The magnitude of the response starts to diverge when the nodal phase is approached from either side, as shown by the results boxed with dashed lines. On the other hand, the high-frequency behavior (not depicted here) remains the same in all phases. See Fig. 2 for a description of the phase diagram in the lower portion of the figure.

Our paper is organized as follows. In Sec. II we introduce our theoretical model. We describe the phases of the model, methods to characterize their topological character, and we present a global phase diagram. We also give the expressions used to compute the nonlinear (second-order) optical response. In Sec. III we describe the main results of our work, showing that it is the low-frequency response that characterizes the superconducting state. Finally, in Sec. IV we present the central conclusions of our work and an outlook for issues for future study. Various technical details of the calculations appear in the Appendixes.

II. MODEL

A. Hamiltonian

We consider a two-dimensional (2D) TMD monolayer of tantalum disulfide (1H-TaS_2) on a substrate, which breaks inversion and mirror symmetry. We use the density functional theory based six-band tight-binding model provided in Ref. [82]. The system can be described by three orbital degrees of freedom d_{z^2}, $d_{x^2-y^2}$, and d_{xy}, along with two spin degrees of freedom. The substrate plays an important role as it breaks the mirror symmetry of the z-axis (M_z), but mirror symmetry about the x-axis (M_x) and symmetry under rotation by 120° about the z-axis (C_3) remain.

The single-particle Hamiltonian $H_0(\mathbf{k})$, Eq. (A1), describing this system is formulated using a tight-binding model considering on-site pairings and up to third-nearest-neighbor hopping terms. The details of the Hamiltonian and the hopping parameters [82] are given in Appendix A. However, we also consider the case of chemical potential $\mu = 0$ in addition to $\mu = -50\,\text{meV}$ going beyond the regime studied in Ref. [82]. (We note that Ref. [82] did not study any aspects of the optical response of the model.)

One can directly add M_z symmetry-breaking terms to $H_0(\mathbf{k})$, such as a Rashba spin-orbit coupling term,

$$H_{\text{Rashba}}(\mathbf{k}) = i\alpha \sum_{j=1}^{6} \left(R_j^x \sigma_y - R_j^y \sigma_x\right) e^{i\mathbf{R}_j\cdot\mathbf{k}} \otimes \mathbb{I}_3, \qquad (1)$$

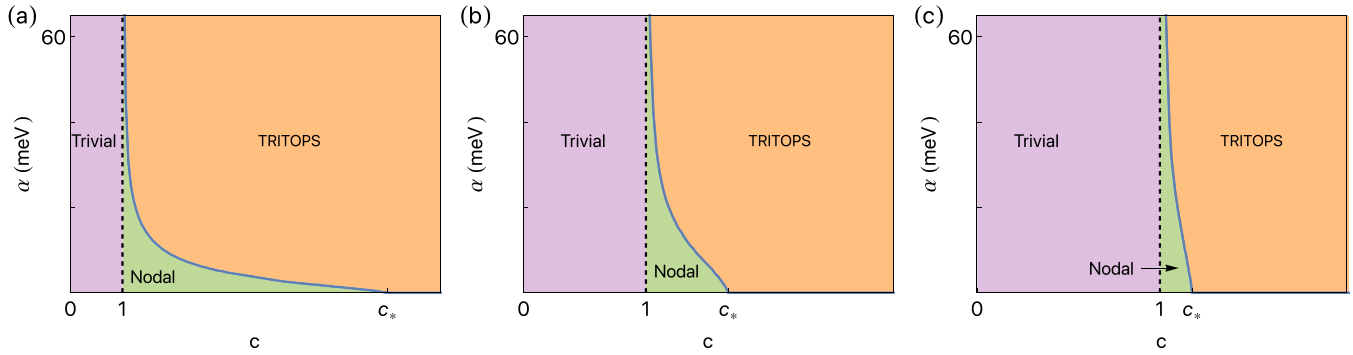

FIG. 2. Phase diagram in the α-c plane for $\mu = 0$ and (a) $\Delta_1 = 10\,\text{meV}$, $c_* = 6.054$; (b) $\Delta_1 = 45\,\text{meV}$, $c_* = 1.665$; (c) $\Delta_1 = 100\,\text{meV}$, $c_* = 1.1705$. Smaller Δ_1 values (which set the scale of the superconducting transition temperature) are closer to experimental values for superconducting TMDs. For smaller Δ_1 the c values over which the nodal phase is possible are enlarged, but the phase is more easily destroyed by spin-orbit coupling, whose strength is given by α.

where σ_x, σ_y are Pauli matrices, $\mathbf{R}_j$ are the lattice vectors for nearest-neighbor sites, $\mathbb{I}_3$ is the 3×3 identity matrix, and α is a constant describing the strength of the Rashba term. This time-reversal invariant term plays an important role in controlling the phase of the superconducting Hamiltonian.

Superconductivity is incorporated via the Bogoliubov–de Gennes formalism, with the 12×12 superconducting Hamiltonian given by

$$H_{\text{SC}}(\mathbf{k}) = \begin{bmatrix} H_0(\mathbf{k}) & \Delta \\ \Delta^\dagger & -H_0(-\mathbf{k})^T \end{bmatrix}, \tag{2}$$

which is written in the Nambu basis $\Psi_{\mathbf{k}}^\dagger = (\psi_{\mathbf{k}}^\dagger, \psi_{-\mathbf{k}}^T)$ with

$$\psi_{\mathbf{k}}^T = (d_{z^2,\uparrow}, d_{xy,\uparrow}, d_{x^2-y^2,\uparrow}, d_{z^2,\downarrow}, d_{xy,\downarrow}, d_{x^2-y^2,\downarrow}), \tag{3}$$

where $d_{\nu,\sigma}(\mathbf{k})$ are annihilation operators acting on electrons with spin σ in orbital ν. In Eq. (2), Δ is a momentum-*independent* pairing matrix determined from symmetries of the model.

The anticommutativity of fermions generally requires $\Delta(\mathbf{k}) = -\Delta^T(-\mathbf{k})$. In a momentum-independent matrix, we thus have $\Delta = -\Delta^T$. In a single-orbital system, this requirement eliminates all but the trivial $i\sigma_y$ term from the pairing matrix. However, the additional degrees of freedom contained within a multiorbital system allow other terms, provided the pairing matrix remains antisymmetric in the orbital degree of freedom. The most general form of the pairing matrix consistent with the symmetries of the system is given by [82]

$$\Delta = \begin{bmatrix} 0 & \Delta_4 & i\Delta_4 & \Delta_1 & 0 & 0 \\ -\Delta_4 & 0 & 0 & 0 & \Delta_2 & i\Delta_3 \\ -i\Delta_4 & 0 & 0 & 0 & -i\Delta_3 & \Delta_2 \\ -\Delta_1 & 0 & 0 & 0 & \Delta_4 & -i\Delta_4 \\ 0 & -\Delta_2 & i\Delta_3 & -\Delta_4 & 0 & 0 \\ 0 & -i\Delta_3 & -\Delta_2 & i\Delta_4 & 0 & 0 \end{bmatrix}, \tag{4}$$

where $\Delta_{1,2,3,4}$ are real parameters. Here, Δ_1 describes intraorbital singlet pairing in the d_{z^2} orbital, while Δ_2 describes intraorbital singlet pairing within the $d_{x^2-y^2}$ and d_{xy} (in-plane) orbitals. Similarly, Δ_3 gives the interorbital triplet pairing of the d_{xy} and $d_{x^2-y^2}$ orbitals. The parameter Δ_4 is also an interorbital triplet term and gives the pairing of same-spin states. In our numerical analysis of the nonlinear optical response, we set $\Delta_2 = \Delta_1$ and $\Delta_3 = 0$. The ratio $c = \frac{\Delta_4}{\zeta \Delta_1}$, where ζ is a model-dependent parameter, is an important quantity controlling the phase of the model. The pair of quantities (c, α) can be varied to drive the system across the different phases as discussed in Fig. 2 and Sec. II B. This model has successfully explained the crystal orientation-dependent local density of states of edge modes observed in scanning tunneling microscope experiments [63].

B. Phases and topology

The model described with the pairing matrix given in Eq. (4) shows three distinct phases—trivial, nodal, and TRITOPS. The trivial and TRITOPS phases are gapped, and based on the symmetry class of the system they can be distinguished with a $\mathbb{Z}_2$ invariant [82]. One can compute the invariant by putting H_{SC} in an off-diagonal block form. To do this, we first change the basis of the hole block of the BdG spinor, following the work of Ref. [82],

$$\widetilde{\Psi} = \begin{bmatrix} \mathbb{I}_2 \otimes \mathbb{I}_3 & 0 \\ 0 & i\sigma_y \otimes \mathbb{I}_3 \end{bmatrix} \begin{bmatrix} \psi_{\mathbf{k}} \\ \psi_{-\mathbf{k}}^\dagger \end{bmatrix}. \tag{5}$$

The Hamiltonian in the transformed basis, $\widetilde{H}_{\text{SC}}(\mathbf{k})$, can then be expressed in the off-diagonal form,

$$e^{i\frac{\pi}{4}\tau_x} \widetilde{H}_{\text{SC}}(\mathbf{k}) e^{-i\frac{\pi}{4}\tau_x} = \begin{bmatrix} 0 & Q_{\mathbf{k}} \\ Q_{\mathbf{k}}^\dagger & 0 \end{bmatrix}, \tag{6}$$

where τ_x is a Pauli matrix in the particle-hole subspace. The matrix $Q_{\mathbf{k}}$ is related to the single-particle Hamiltonian and the pairing matrix as

$$iQ_{\mathbf{k}} = H_0(\mathbf{k}) + iU_{\mathcal{T}}\Delta^\dagger, \tag{7}$$

where $U_{\mathcal{T}} = i\sigma_y \otimes \mathbb{I}_3$. With $Q_{\mathbf{k}}$, the $\mathbb{Z}_2$ invariant can be explicitly calculated following Ref. [97]. However, in the weak pairing limit, when Δ is tiny compared to the energy separation between bands, one can calculate the topological invariant by simply looking at the sign of the effective pairing $\delta_{n,\mathbf{k}}$ for bands crossing the Fermi level. The effective pairing is defined

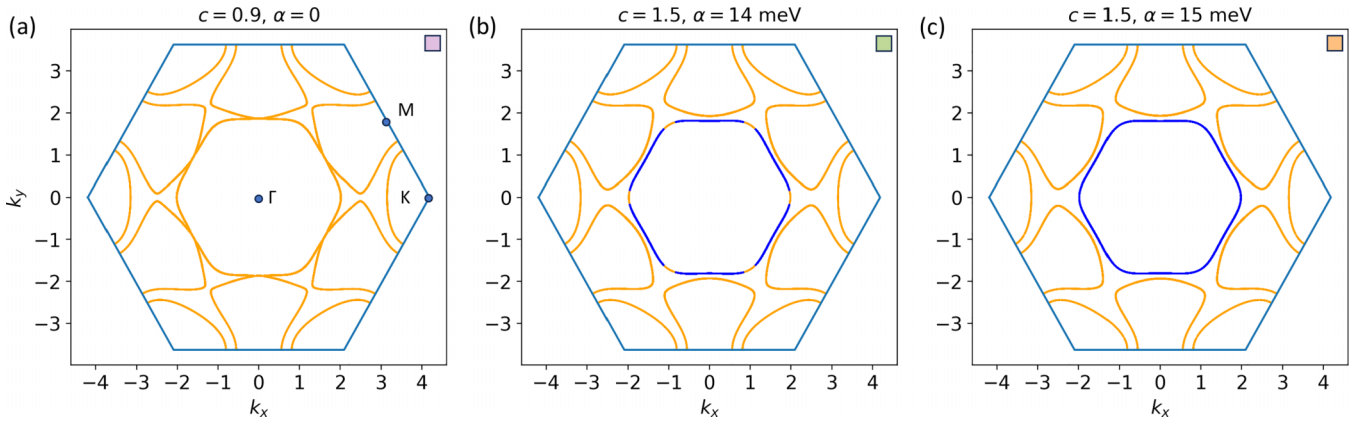

FIG. 3. Sign of the effective pairing for the (a) trivial, (b) nodal, (c) and TRITOPS phases, where blue (orange) corresponds to -1 ($+1$). We used $\Delta_1 = 10$ meV and $\mu = -50$ meV for these plots. Note that for $c = 1.5$, $\alpha_c = 14.58$ meV. The small colored square box in the upper right corner of each subpanel in the figure corresponds to the phase of the same color in Fig. 2.

as

$$\delta_{n,\mathbf{k}} = \langle n, \mathbf{k}| U_{\mathcal{T}} \Delta^{\dagger} |n, \mathbf{k}\rangle \,, \tag{8}$$

where $|n, \mathbf{k}\rangle$ is an eigenstate of $H_0(\mathbf{k})$. In this limit, the system is topological if there are an odd number of Fermi pockets, each enclosing one TRIM point and with a negative $\delta_{n,\mathbf{k}}$ [97]. Since this invariant is only well defined when the system is gapped, in the nodal phase it is sometimes useful to look at the characteristic angle, $\theta_{\mathbf{k}}$, defined as

$$\theta_{\mathbf{k}} = \arg(\det Q_{\mathbf{k}}), \tag{9}$$

whose winding around a node gives its topological charge. As seen in Fig. 2, the trivial to nodal phase transition can only be driven with $c = \frac{\Delta_4}{\zeta \Delta_1}$. The parameter ζ used in the definition is chosen such that $c = 1$ is the transition point from the trivial to the nodal phase at $\mu = 0$. When entering the nodal phase, the nodes appear on the innermost Fermi surface (of the normal Hamiltonian) along the Γ-M lines. (See Fig. 3.) When c is increased further, each node splits into two and start to move away from their origin point (but stays on the same Fermi surface due to time-reversal symmetry [98–100]). At $c = c_*$, oppositely charged nodes merge on that Fermi surface, along the Γ-K lines, marking a transition to the gapped TRITOPS phase. We should note that once in the nodal phase ($1 < c < c_*$), it is possible to drive the system into the TRITOPS phase by turning on α. Increasing α causes the nodes to move along the Fermi surface as before and finally merge along the Γ-K lines at $\alpha = \alpha_c$. In fact, Δ_1 and c_* are inversely proportional, making the α driven nodal to TRITOPS phase transition more accessible for values of pairing amplitudes used for 1H-TMDs in Ref. [82].

With this picture of node creation and annihilation in mind, one can determine the two phase boundaries by looking at the gap closing along the Γ-M and the Γ-K lines. Phase diagrams obtained using this approach are shown in Fig. 2 for three different values of the intraorbital pairing term Δ_1. These phase transitions can also be confirmed by looking at the sign of the effective pairing on the Fermi surface across the phase boundaries, as shown in Fig. 3. In the trivial phase shown in Fig. 3(a), the Fermi surface around all four TRIM points has a positive sign for the effective pairing. On the other hand, for the TRITOPS phase shown in Fig. 3(c), the Fermi pocket around the Γ point acquires a negative sign which indicates the nontrivial nature of this phase. Some of the phase transition points considered in our nonlinear conductivity calculations are given in Tables I and II for the chemical potentials $\mu = 0$ and -50 meV, respectively. Note that for $\mu = -50$ meV the trivial to nodal phase transition point does not change significantly from $c = 1$.

C. Nonlinear optical response

We study the second-order dc response, also known as the photogalvanic effect, following Refs. [32,33]. Using the expression for the second-order

TABLE I. Various nodal to TRITOPS phase transition points for $\mu = 0$ for different values of Δ_1. Note that at zero doping, the trivial to nodal transition is always at $c = 1$ by construction.

Δ_1 (meV)	ζ	c	α_c (meV)
10	1.171478265857	1.5	13.31677465
		6.05433710	0
45	1.170919255973	1.3	13.452
		1.66527725	0
100	1.168647137	1.17054149	0

TABLE II. Various phase transition points for $\mu = -50$ meV for different Δ_1 (the respective ζ value is kept the same as for $\mu = 0$).

Δ_1 (meV)	Transition	c	α_c (meV)
10	Trivial → Nodal	1.0087	
	Nodal → TRITOPS	1.5	14.58
45	Trivial → Nodal	1.00194861	
	Nodal → TRITOPS	1.3	15.62597
	Nodal → TRITOPS	1.7917638	0

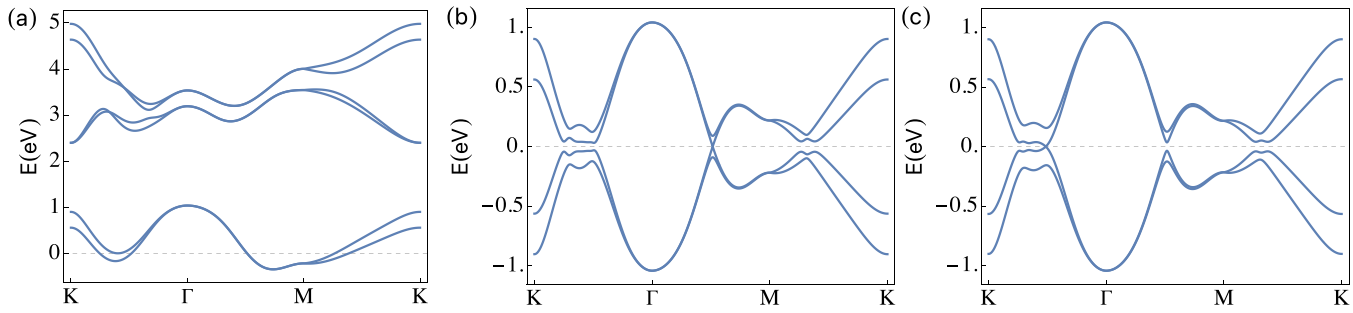

FIG. 4. Band structure for the single-particle Hamiltonian H_0 without Rashba SOC at $\mu = -50$ meV is shown in (a). The energy bands close to the Fermi energy for the Bogoliubov–de Gennes Hamiltonian $H_{\rm SC}$ with $\Delta_1 = 45$ meV for (b) $c = 1.001\,948\,6$, $\alpha = 0$ and (c) $c = 1.791\,763\,8$, $\alpha = 0$ are also shown for the same chemical potential. One can see a gap closing along the Γ-M line at the trivial-nodal and along the Γ-K line at the nodal-TRITOPS phase transition points in (b) and (c), respectively.

conductivity,

$$\sigma^{\alpha\beta\gamma}(\widetilde{\omega};\omega_1,\omega_2) = \int_{\rm FBZ}\frac{d^2k}{(2\pi)^2}\frac{1}{2(i\omega_1-\eta)(i\omega_2-\eta)}\Bigg[\sum_a\frac{1}{2}J^{\alpha\beta\gamma}_{aa}f_a+\sum_{a,b}\frac{1}{2}\left(\frac{J^{\alpha\beta}_{ab}J^{\gamma}_{ba}f_{ab}}{\omega_2+i\eta-E_{ba}}+\frac{J^{\alpha\gamma}_{ab}J^{\beta}_{ba}f_{ab}}{\omega_1+i\eta-E_{ba}}\right)$$
$$+\sum_{a,b}\frac{1}{2}\frac{J^{\alpha}_{ab}J^{\beta\gamma}_{ba}f_{ab}}{\widetilde{\omega}+2i\eta-E_{ba}}+\sum_{a,b,c}\frac{1}{2}\frac{J^{\alpha}_{ab}}{\widetilde{\omega}+2i\eta-E_{ba}}\left(\frac{J^{\beta}_{bc}J^{\gamma}_{ca}f_{ac}}{\omega_2+i\eta-E_{ca}}-\frac{J^{\beta}_{ca}J^{\gamma}_{bc}f_{cb}}{\omega_2+i\eta-E_{bc}}\right)$$
$$+\sum_{a,b,c}\frac{1}{2}\frac{J^{\alpha}_{ab}}{\widetilde{\omega}+2i\eta-E_{ba}}\left(\frac{J^{\gamma}_{bc}J^{\beta}_{ca}f_{ac}}{\omega_1+i\eta-E_{ca}}-\frac{J^{\gamma}_{ca}J^{\beta}_{bc}f_{cb}}{\omega_1+i\eta-E_{bc}}\right)\Bigg], \tag{10}$$

where $\widetilde{\omega} = \omega_1 + \omega_2$, we calculate the photogalvanic response by computing the dc conductivities $\sigma^{\alpha\beta\gamma}(0;\omega,-\omega)$. In Figs. 6–8 we plot $\sigma^{\alpha\beta\gamma}(0;\omega,-\omega)$ as a function of ω. Here, J^{α}_{ab}, $J^{\alpha\beta}_{ab}$, and $J^{\alpha\beta\gamma}_{ab}$ are matrix elements of the generalized current operator J defined as [32,33]

$$J^{\alpha_1,\alpha_2,\ldots,\alpha_n} = (-1)^n\frac{\partial^n H_{\rm SC}(\mathbf{k},\boldsymbol{\lambda})}{\partial\lambda^{\alpha_1}\partial\lambda^{\alpha_2}\cdots\partial\lambda^{\alpha_n}}\bigg|_{\boldsymbol{\lambda}=0}, \tag{11}$$

where

$$H_{SC}(\mathbf{k},\boldsymbol{\lambda}) = \begin{bmatrix} H_0(\mathbf{k}-\boldsymbol{\lambda}) & \Delta \\ \Delta^\dagger & -H_0(-\mathbf{k}-\boldsymbol{\lambda})^T \end{bmatrix}. \tag{12}$$

To numerically evaluate Eq. (10), the integral is converted to a sum over discrete **k**-points in the first Brillouin zone of the system. Latin indices label the eigenvectors of $H_{\rm SC}(\mathbf{k})$ with $E_{ab} = E_a - E_b$ and $f_{ab} = f_a - f_b$, where f_a refers to the Fermi-Dirac distribution function $f_a = 1/(1+e^{E_a/k_BT})$. We take $T = 10^{-4}$K and a small phenomenological scattering rate $\eta = 5\times10^{-4}$ eV for $\Delta_1 = 100$, 45 meV and $\eta = 1.5\times10^{-4}$ eV for $\Delta_1 = 10$ meV. Note that these pairing amplitudes are about 10–100 times larger that the one given in Ref. [82], which are around 1 meV. Working with pairings on the order of 1 meV results in unreliable numerical results unless one uses an extremely fine k-grid, which in turn leads to high computational time. To overcome this, we work with large pairing amplitudes instead and then show that decreasing them has a clear trend in terms of certain features that are of interest to us, such as the low-frequency behavior. One can then safely extrapolate the trends down to pairing on the order of meV. (Such trends are also reflected in the critical boundaries of the phase diagrams themselves, as seen in Fig. 2 and Tables I and II.) The sign of the divergence in the low-frequency regime is what provides the strongest fingerprint of different superconducting phases.

For comparison we also examine the first-order conductivity of the system, given by [32]

$$\sigma^{\alpha\beta}(\omega) = \frac{i}{2(\omega+i\eta)}\sum_{a,b}\left(\frac{J^{\alpha}_{ab}J^{\beta}_{ba}f_{ab}}{\omega+i\eta-E_{ba}}+J^{\alpha\beta}_{ab}f_a\delta_{ab}\right), \tag{13}$$

for signatures of the topological phases of the system. We find that the second-order response in Eq. (10) reflects the superconducting phase and transitions between phases while the first-order response in Eq. (13) does not. This physical result provides an excellent example of additional physics being obtained though higher-order responses.

III. RESULTS

We study the second-order, Eq. (10), and the first-order, Eq. (13), optical responses in two different frequency ranges—one on the order of the superconducting gap, and the other much above it. The focus on the low-energy window is motivated by the size of the superconducting terms in Eq. (2) and hence captures the role of transitions between particle and hole copies of bands near the Fermi energy. These transitions rely on nonzero superconducting pairing terms and their parity. On the other hand, for the higher-energy window,

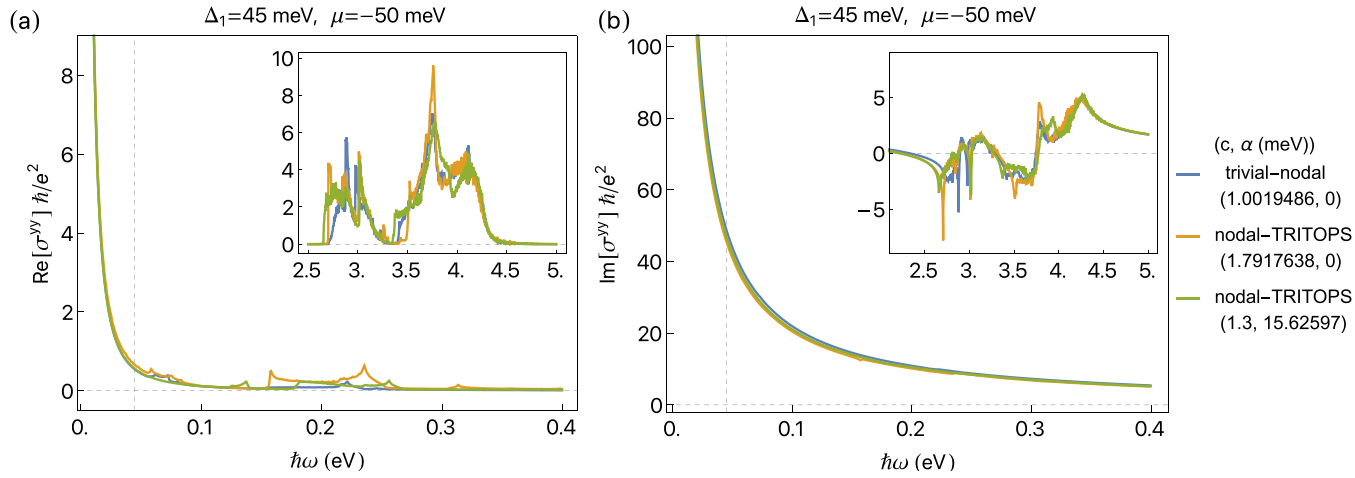

FIG. 5. The real and imaginary part of first-order conductivity $\sigma^{xx}(\omega) = \sigma^{yy}(\omega)$ for $\Delta_1 = 45\,\text{meV}$ and $\mu = -50\,\text{meV}$. Both the low- and high-frequency response remain unchanged across the trivial-nodal and nodal-TRITOPS phase transitions points.

the optical response arises mainly from transitions between different single-particle bands. The band structures for the normal and the superconducting Hamiltonians are shown in Fig. 4.

The real and imaginary parts of the first-order conductivity, Eq. (13), are shown in Fig. 5 for $\Delta_1 = 45\,\text{meV}$ and chemical potential, $\mu = -50\,\text{meV}$ in the two frequency windows. The electric field of the linearly polarized light is taken to be in the y-direction. We see no features indicating a phase transition in the linear conductivity. For our system, $\sigma^{xx} = \sigma^{yy}$ whereas $\sigma^{xy} = 0$ due to the presence of time-reversal symmetry.

The second-order conductivity results obtained from Eq. (10) are shown in Figs. 6–8. Unlike the linear conductivity, the σ^{yyy} (again, the electric field is taken to be in the y-direction for linearly polarized light and one has $\sigma^{yxx} = -\sigma^{yyy}$ due to threefold rotation symmetry) component of the second-order conductivity shows distinct signatures when

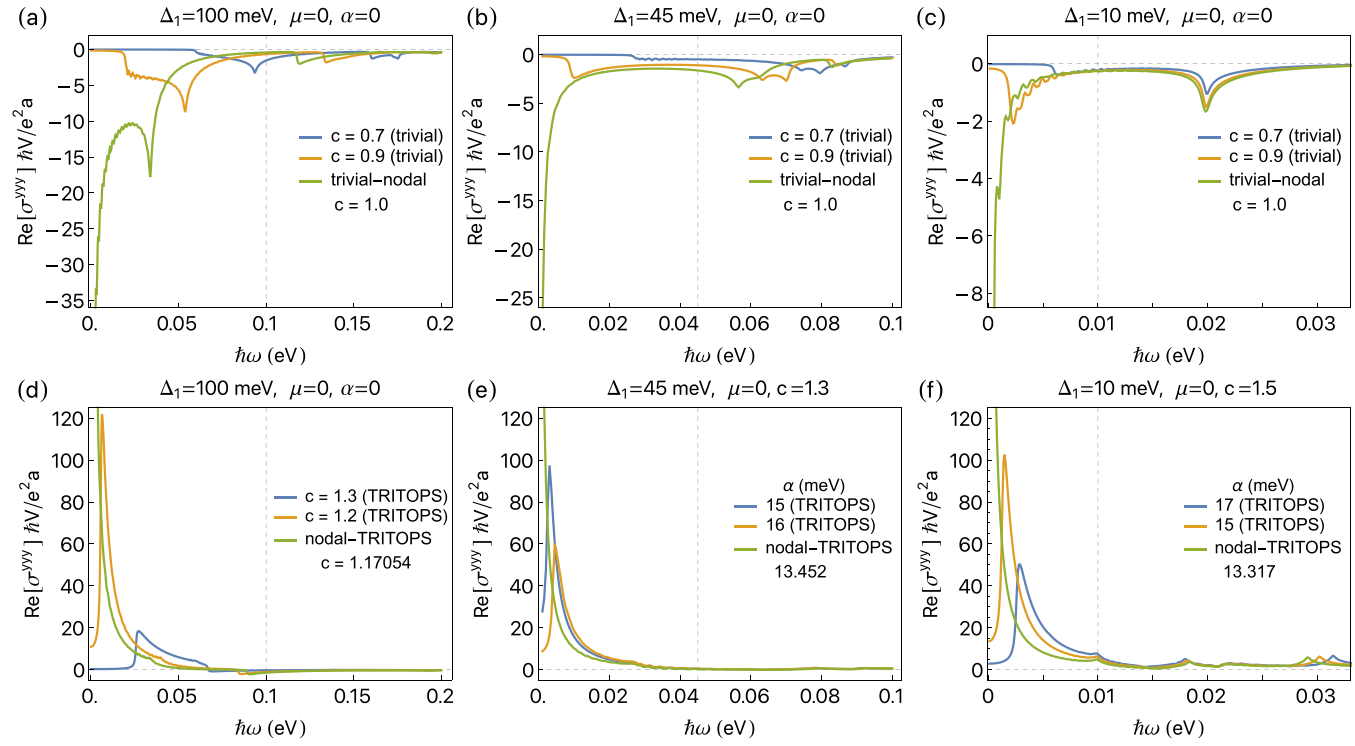

FIG. 6. $\text{Re}[\sigma^{yyy}(\omega)]$ for different values of Δ_1, c, and α for $\mu = 0$. Panels (a)–(c) show the behavior when approaching the trivial-nodal phase boundary, whereas (d)–(f) capture the behavior past the nodal-TRITOPS phase boundary. Close to the phase boundary, the sign of the low-frequency photogalvanic response in the trivial and TRITOPS phase matches that of the divergence. Note that we chose to drive the nodal to TRITOPS phase transition with c in (d) and α in (e), (f), showing no qualitative difference. The vertical dashed line in each figure indicates the value of Δ_1. The factor a appearing in the y-axis label is the lattice constant for the 1H-TaS_2 monolayer.

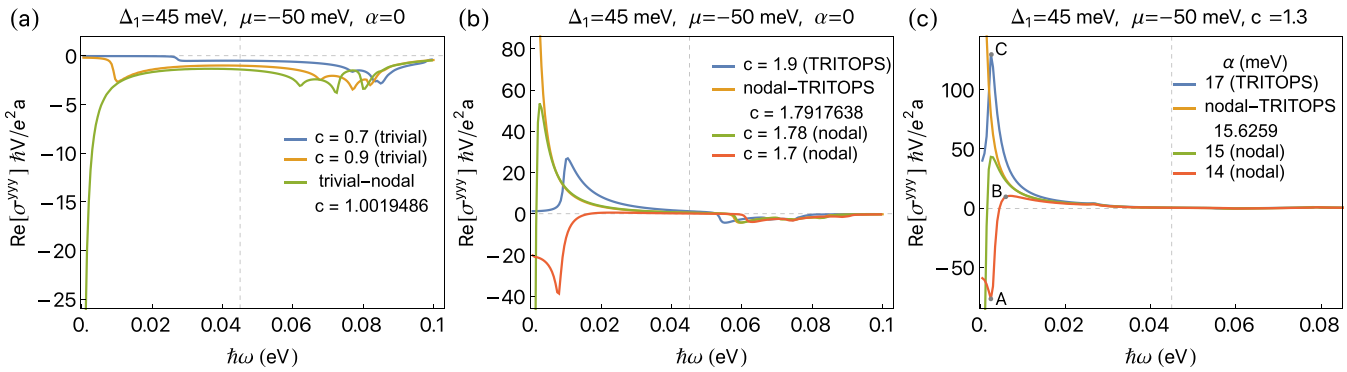

FIG. 7. $\mathrm{Re}[\sigma^{yyy}(\omega)]$ for $\Delta_1 = 45\,\mathrm{meV}$ and $\mu = -50\,\mathrm{meV}$. Panel (a) shows the behavior when approaching the trivial-nodal phase boundary. Panels (b) and (c) capture the behavior across the nodal-TRITOPS phase boundary for c and α driven transitions, respectively. Again, we see no qualitative difference between the two routes. The vertical dashed line indicates the value of Δ_1.

approaching the nodal phase from the trivial and the TRITOPS phases in the low-frequency regime ($\omega \lesssim \Delta_1$). In particular, $\mathrm{Re}[\sigma^{yyy}]$ shows a zero-frequency divergence at the trivial to nodal phase transition, as shown in Figs. 6(a)–6(c) and 7(a) for different values of Δ_1 and chemical potential. However, at the TRITOPS to nodal phase transition, there is an opposite sign zero-frequency divergence as shown in Figs. 6(d)–6(f) and Figs. 7(b) and 7(c). We also find that close to the two phase boundaries, the sign of the low-frequency photogalvanic response in the trivial and TRITOPS phases matches with that of the divergence. For the trivial phase this behavior is captured in Figs. 6(a)–6(c), whereas for the TRITOPS phase it is shown in Figs. 6(d)–6(f). This behavior remains qualitatively unchanged when we decrease Δ_1 from 100 to 45 meV, and finally to 10 meV. We note that the behavior of σ^{yyy} across the nodal-TRITOPS phase boundary does not depend on whether the transition was driven by c or α, making it a useful signature of the phase transition itself.

We also note that σ^{yyy}'s approach to the divergences at the nodal phase boundaries is different from within the nodal phase and from the outside. While the trivial and TRITOPS phase conductivities' approach to their respective divergences is gradual, the nodal phase conductivity shows a rapid sign change close to the phase boundaries. For the nodal-TRITOPS phase boundary, this can be seen in Figs. 7(b) and 7(c). The nodal phase conductivity develops two peaks [marked as A and B in Fig. 7(c)]. Peaks A and B get closer to the $\omega = 0$ line while becoming increasingly negative and positive, respectively, as the system approaches the transition point. As the system moves closer to the phase boundary, Peak A (now indistinguishable from $\mathrm{Re}[\sigma^{yyy}(0;0,0)]$) rapidly moves up and merges with B to give the divergence at the nodal-TRITOPS phase boundary. More details about the behavior of $\mathrm{Re}[\sigma^{yyy}(0;0,0)]$ are given in Appendix B. We emphasize that just like the TRITOPS phase conductivity peak C, the approach of peak B to its divergence is much more gradual compared to A.

We also considered the effect of doping on the second-order conductivity for the $\Delta_1 = 45\,\mathrm{meV}$ case by taking $\mu = -50\,\mathrm{meV}$. Our results are shown in Fig. 7. A finite value of μ increases the critical values of c, α required for either phase transition, as shown in Table II. However, the behavior of σ^{yyy} around the shifted phase transition points remains unchanged from the $\mu = 0$ case seen in Fig. 6.

Finally, Fig. 8 shows that the high-frequency photogalvanic response remains unaffected across the phase transitions for different values of Δ_1 and μ which makes it useful as a reference point for analyzing the relative sign of the low-frequency divergences and responses around them. We find that the high-frequency response is nonzero for $2.6 \lesssim \omega \lesssim 4.3$ eV. For most of this window, the response is of the same sign as the divergence at the trivial-nodal phase transition point.

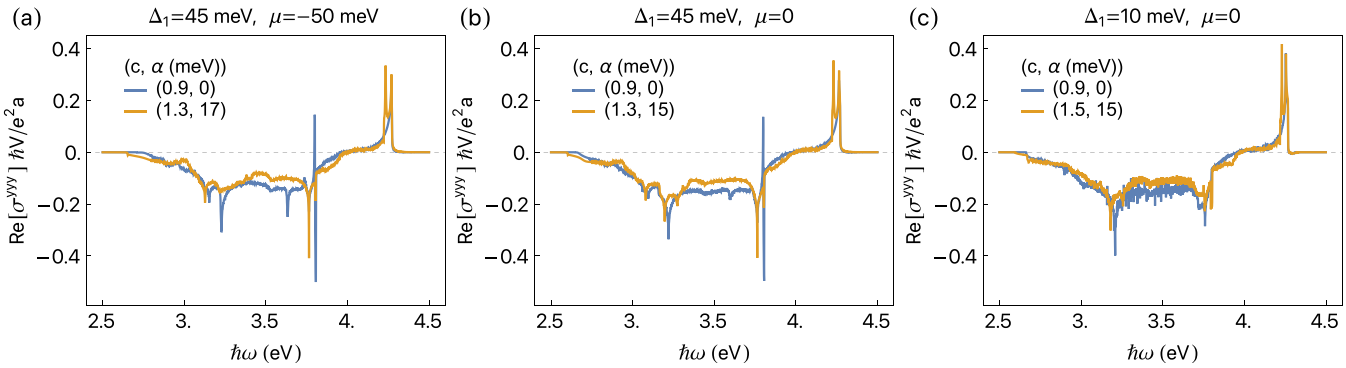

FIG. 8. $\mathrm{Re}[\sigma^{yyy}(\omega)]$ at higher frequencies in the trivial (blue) and TRITOPS (orange) phases for different values of Δ_1 and μ. There is no significant change with changing either μ (a), (b) or Δ_1 (b), (c).

Since the divergence at the nodal-TRITOPS phase transition is of the opposite sign, this observation can be used to distinguish the trivial and TRITOPS phases in experiments. Whether this is a specific feature of the Hamiltonian we study or is true more generally would require different Hamiltonians with the same phase diagram to be studied. Our main purpose here is to show that for 1H-TaS_2 and 4Hb-TaS_2, for which our model is relevant [82], these features can be used to identify the phase and provide complementary information to other experimental studies [63,86,101]. We hope our work will help inspire experimental groups to undertake this challenge.

IV. CONCLUSIONS

We have presented a thorough—both low-frequency and high-frequency regimes—study of the second-order dc response in 1H-TaS_2, out of which the candidate topological superconducting 4Hb-TaS_2 compound is partially built [63,101]. (The 4Hb-TaS_2 compound is composed of alternating layers of 1H-TaS_2 and 1T-TaS_2.) Based on the ratio of inter- and intraorbital pairing amplitudes and the presence of Rashba spin-orbit coupling permitted by inversion symmetry breaking, the system is known to exist in one of three phases: trivial, nodal, and TRITOPS. We have mapped out the phase boundaries by analyzing the gap closing and reopening at the Fermi level. With the phase diagram in hand, we have numerically calculated the first- and second-order conductivities around these transition points. Our results indicate that the transitions from trivial to nodal phases and from nodal to TRITOPS phases are each characterized by a zero-frequency divergence in the photogalvanic response but with opposite signs. No signature of the superconducting phase of the system is observed in the linear response. This makes the photogalvanic response an effective probe to distinguish the superconducting phases of 1H-TaS_2 and potentially the closely related 4Hb-TaS_2 compound.

The topological phase transition in 1H-TaS_2 depends on the extent of parity mixing in the superconducting pairing and the strength of the Rashba spin-orbit coupling. The parity mixing relies on the symmetry aspects of the substrate (e.g., broken inversion symmetry), and hence the proximity/coupling strength to a substrate can be used as a knob to control the ratio of the two opposite parity components of the superconducting order parameter. The Rashba spin-orbit coupling also arises from broken inversion symmetry, and thus can be possibly varied either by substrate engineering or by applying an out-of-plane electric field, allowing independent control of the parity mixing of the superconducting order parameter and the Rashba spin-orbit coupling.

The superconductivity in 1H-TaS_2 is very robust to an in-plane magnetic field, which may serve as another knob to modify topological properties [102]. In future studies it would be interesting to determine if the quantum phase transitions in the presence of an in-plane magnetic field would also lead to some unique signatures in the second-order dc response.

Further theoretical studies of distinct experimental signatures of topological superconductivity in different measurements can be used to more clearly identify whether a given material indeed supports topological superconductivity, rather than relying on one class of measurements alone. Given the controversy around purported topological superconductors, multiple measurement signatures of topology in superconductors is highly desirable.

TABLE III. Values of the hopping parameters taken from [82].

t_0	t_1	t_2	t_{11}	t_{12}	t_{22}
−0.1917	0.4057	0.4367	0.2739	0.3608	−0.1845
r_0	r_1	r_2	r_{11}	r_{12}	r_{22}
0.0409	−0.069	0.0928	−0.0066	0.1116	0.
u_0	u_1	u_2	u_{11}	u_{12}	u_{22}
0.0405	−0.0324	−0.0141	0.1205	−0.0316	−0.0778
ϵ_0	ϵ_1	ϵ_2	λ_{SO}		
1.6507	2.5703	2.5703	0.1713		

ACKNOWLEDGMENTS

We acknowledge funding from the National Science Foundation through the Center for Dynamics and Control of Materials: an NSF MRSEC under Cooperative Agreements No. DMR-1720595 and No. DMR-2114825. G.A.F. acknowledges additional support from the Alexander von Humboldt Foundation.

APPENDIX A: DETAILS OF MODEL

1. TMD monolayer Hamiltonian

The Hamiltonian for the transition-metal dichalcogenide monolayer without superconductivity is given by

$$H_0(\mathbf{k}) = E + \sum_{j=1}^{6} R_j e^{i\mathbf{R}_j\cdot\mathbf{k}} + \sum_{j=1}^{6} S_j e^{i\mathbf{S}_j\cdot\mathbf{k}} + \sum_{j=1}^{6} T_j e^{i\mathbf{T}_j\cdot\mathbf{k}}, \tag{A1}$$

where $\mathbf{R}_j$, $\mathbf{S}_j$, and $\mathbf{T}_j$ are the first-, second-, and third-nearest-neighbor lattice vectors, respectively, and R_j, S_j, and T_j are the corresponding hopping matrices. E, R_1, S_1, and T_1 are defined as

$$E = \sigma_0 \otimes \begin{bmatrix} \epsilon_0 - \mu & 0 & 0 \\ 0 & \epsilon_1 - \mu & 0 \\ 0 & 0 & \epsilon_2 - \mu \end{bmatrix} + \sigma_z \otimes \begin{bmatrix} 0 & 0 & 0 \\ 0 & 0 & i\lambda_{SO} \\ 0 & -i\lambda_{SO} & 0 \end{bmatrix}, \tag{A2}$$

$$R_1 = \sigma_0 \otimes \begin{bmatrix} t_0 & -t_1 & t_2 \\ t_1 & t_{11} & -t_{12} \\ t_2 & t_{12} & t_{22} \end{bmatrix}, \tag{A3}$$

$$S_1 = \sigma_0 \otimes \begin{bmatrix} r_0 & r_2 & -\frac{1}{\sqrt{3}} r_2 \\ r_1 & r_{11} & r_{12} \\ -\frac{1}{\sqrt{3}} r_1 & r_{12} & \left(r_{11} + \frac{2}{\sqrt{3}} r_{12}\right) \end{bmatrix}, \tag{A4}$$

$$T_1 = \sigma_0 \otimes \begin{bmatrix} u_0 & -u_1 & u_2 \\ u_1 & u_{11} & -u_{12} \\ u_2 & u_{12} & u_{22} \end{bmatrix}, \tag{A5}$$

whereas the remaining hopping matrices can be generated via the following:

$$C_3 = \begin{bmatrix} e^{-i\frac{\pi}{3}} & 0 \\ 0 & e^{i\frac{\pi}{3}} \end{bmatrix} \otimes \begin{bmatrix} 1 & 0 & 0 \\ 0 & -\frac{1}{2} & \frac{\sqrt{3}}{2} \\ 0 & -\frac{\sqrt{3}}{2} & -\frac{1}{2} \end{bmatrix}, \tag{A6}$$

$$\begin{aligned} R_2 &= C_3^\dagger R_1^\dagger C_3 \quad S_2 = C_3^\dagger S_1^\dagger C_3 \quad T_2 = C_3^\dagger T_1^\dagger C_3 \\ R_3 &= C_3 R_1 C_3^\dagger \quad S_3 = C_3 S_1 C_3^\dagger \quad T_3 = C_3 T_1 C_3^\dagger \\ R_4 &= R_1^\dagger \quad S_4 = S_1^\dagger \quad T_4 = T_1^\dagger \\ R_5 &= C_3^\dagger R_1 C_3 \quad S_5 = C_3^\dagger S_1 C_3 \quad T_5 = C_3^\dagger T_1 C_3 \\ R_6 &= C_3 R_1^\dagger C_3^\dagger \quad S_6 = C_3 S_1^\dagger C_3^\dagger \quad T_6 = C_3 T_1^\dagger C_3^\dagger \end{aligned} \tag{A7}$$

The hopping parameters are given in Table III.

APPENDIX B: ZERO-FREQUENCY DIVERGENCE IN RE[σ^{yyy}]

We set $\omega_1 = -\omega_2 = 0$ and look at the integrand of $\sigma^{yyy}(0;0,0)$ from Eq. (10). After some simplification, we obtain

$$\begin{aligned} &\frac{1}{2\eta^2}\Bigg[\sum_a \frac{1}{2} J^{yyy}_{aa} f_a \\ &+ \sum_{a,b} \frac{1}{2} J^{yy}_{ab} J^{y}_{ba} f_{ab} \left(\frac{2}{i\eta - E_{ba}} - \frac{1}{2i\eta + E_{ba}}\right) \\ &+ \sum_{a,b,c} \frac{J^{y}_{ab} J^{y}_{bc} J^{y}_{ca}}{2i\eta - E_{ba}} \left(\frac{f_{ac}}{i\eta - E_{ca}} - \frac{f_{cb}}{i\eta - E_{bc}}\right)\Bigg]. \end{aligned} \tag{B1}$$

It is easily seen that the integrand is real. To simplify it further, we set $T = 0$K, so $f_a = 1 - \theta(E_a)$ and $f_{ab} = \theta(E_b) - \theta(E_a)$, where $\theta(x)$ is the Heaviside step function. The structure of the Bogoliubov–de Gennes Hamiltonian is such that it has symmetric eigenvalues with respect to zero energy. If the eigenvalues are sorted in ascending order at each k-point (bands labeled 0–11), then only bands 5 and 6 are important for capturing the divergence since they are the bands closest to zero energy. Picking out terms involving these bands from Eq. (B1), we get

$$\begin{aligned} &\frac{1}{2\eta^2}\Bigg[\frac{1}{2} J^{yyy}_{55} + \mathrm{Re}\left[J^{yy}_{56} J^{y}_{65}\left(\frac{2}{i\eta - 2E_6} - \frac{1}{2i\eta + 2E_6}\right)\right] \\ &+ \mathrm{Re}\left[\frac{J^{y}_{56} J^{y}_{65}}{i\eta + E_6} \frac{J^{y}_{66} - J^{y}_{55}}{i\eta + 2E_6}\right] + J^{y}_{56} J^{y}_{65}\left(\frac{J^{y}_{66} - J^{y}_{55}}{\eta^2 + 4E_6^2}\right) \\ &+ \frac{J^{y}_{56} J^{y}_{65}}{2}\left(\frac{J^{y}_{66} - J^{y}_{55}}{(i\eta + 2E_6)^2} + \frac{J^{y}_{66} - J^{y}_{55}}{(i\eta - 2E_6)^2}\right)\Bigg]. \end{aligned} \tag{B2}$$

One has $J^{yyy}_{55}(\mathbf{k}) = -J^{yyy}_{55}(-\mathbf{k})$ and $J^{y}_{55}(\mathbf{k}) = J^{y}_{66}(\mathbf{k})$. The first term contributes nothing when integrated [note $E_a(\mathbf{k}) = E_a(-\mathbf{k})$], whereas the third, fourth, and fifth terms are zero. Thus, only the second term remains,

$$\int_{E_6(\mathbf{k})<\epsilon} \frac{d^2k}{8\pi^2\eta^2} \mathrm{Re}\left[J^{yy}_{56} J^{y}_{65}\left(\frac{2}{i\eta - 2E_6} - \frac{1}{2i\eta + 2E_6}\right)\right], \tag{B3}$$

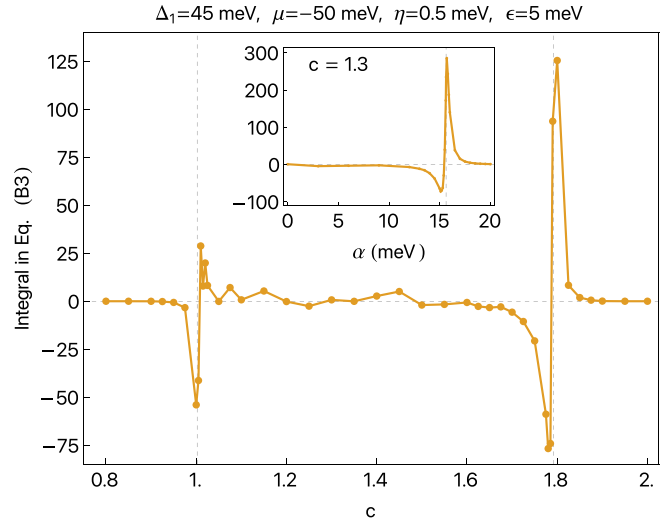

FIG. 9. Behavior of the integral in Eq. (B3) across the trivial-nodal ($c = 1.001\,948\,6$) and nodal-TRITOPS ($c = 1.791\,763\,8$) phase transition points. Inset: Behavior of the same integral across the nodal-TRITOPS phase boundary when the transition is driven by α. Note that for $c = 1.3$, $\alpha_c = 15.6259$ meV.

where ϵ is a small cutoff (staying close to the Fermi level where the low-energy approximation is reliable). Near the node there is a Dirac-like dispersion, and small ϵ keeps one within the linear regime. The divergence of the integral is numerically shown in Fig. 9 as a function of the parameter c and α which controls the phase of the superconductor. The structure of the divergences is consistent with the conductivity plots in Fig. 7, providing a clearer picture of its origin.

To understand what determines the sign of the divergence, we look at $J^{yy}_{56} J^{y}_{65}$ and find that its real part is zero. This allows further simplification of the integral in Eq. (B3) to

$$\int_{E_6(\mathbf{k})<\epsilon} \frac{d^2k}{8\pi^2} \frac{3\eta\,\mathrm{Im}\left[J^{yy}_{56} J^{y}_{65}\right]}{2\left(\eta^2 + E_6^2\right)\left(\eta^2 + 4E_6^2\right)}, \tag{B4}$$

which shows that the sign of the divergence is determined by the net contribution of $\mathrm{Im}[J^{yy}_{56} J^{y}_{65}]$ around the nodes, as shown in Fig. 10. This term appears in the shift conductivity after one expresses the covariant derivative of the Berry connection in

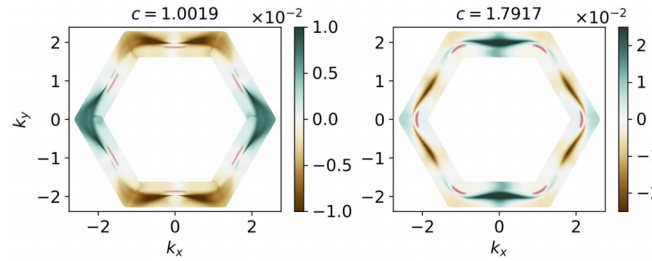

FIG. 10. k-space density plot of $\mathrm{Im}[J^{yy}_{56}\, J^{y}_{65}]$ around the nodes at the phase transition points shown in Fig. 9 ($\alpha = 0$). The red regions correspond to the set of k points that satisfy $E_6(\mathbf{k}) < 5$ meV. Note that the nodes change positions, from being on the Γ-M lines to Γ-K lines, as expected.

its formula in terms of the generalized velocity operators [32]. It can also be written as $J^y_{56}J^y_{65}\,\mathrm{Im}[J^{yy}_{56}/J^y_{56}]$ where the prefactor is the quantum metric and the remaining part can be identified as the Christoffel symbol of the second kind [19]. Since $J^y_{56}J^y_{65}$ is non-negative, we can conclude that the sign is determined by the contribution of $\mathrm{Im}[J^{yy}_{56}/J^y_{56}]$ around the nodes.

[1] V. Belinicher and B. I. Sturman, The photogalvanic effect in media lacking a center of symmetry, Sov. Phys. Usp. **23**, 199 (1980).

[2] J. Orenstein, J. Moore, T. Morimoto, D. Torchinsky, J. Harter, and D. Hsieh, Topology and symmetry of quantum materials via nonlinear optical responses, Annu. Rev. Condens. Matter Phys. **12**, 247 (2021).

[3] T. Morimoto, S. Kitamura, and N. Nagaosa, Geometric aspects of nonlinear and nonequilibrium phenomena, J. Phys. Soc. Jpn. **92**, 072001 (2023).

[4] Q. Ma, A. G. Grushin, and K. S. Burch, Topology and geometry under the nonlinear electromagnetic spotlight, Nat. Mater. **20**, 1601 (2021).

[5] Q. Ma, R. Krishna Kumar, S.-Y. Xu, F. H. Koppens, and J. C. Song, Photocurrent as a multiphysics diagnostic of quantum materials, Nat. Rev. Phys. **5**, 170 (2023).

[6] F. de Juan, A. G. Grushin, T. Morimoto, and J. E. Moore, Quantized circular photogalvanic effect in Weyl semimetals, Nat. Commun. **8**, 15995 (2017).

[7] P. Bhalla, A. H. MacDonald, and D. Culcer, Resonant photovoltaic effect in doped magnetic semiconductors, Phys. Rev. Lett. **124**, 087402 (2020).

[8] A. M. Cook, B. M. Fregoso, F. De Juan, S. Coh, and J. E. Moore, Design principles for shift current photovoltaics, Nat. Commun. **8**, 1 (2017).

[9] H. Watanabe and Y. Yanase, Chiral photocurrent in parity-violating magnet and enhanced response in topological antiferromagnet, Phys. Rev. X **11**, 011001 (2021).

[10] D. E. Parker, T. Morimoto, J. Orenstein, and J. E. Moore, Diagrammatic approach to nonlinear optical response with application to Weyl semimetals, Phys. Rev. B **99**, 045121 (2019).

[11] L. Wu, S. Patankar, T. Morimoto, N. L. Nair, E. Thewalt, A. Little, J. G. Analytis, J. E. Moore, and J. Orenstein, Giant anisotropic nonlinear optical response in transition metal monopnictide Weyl semimetals, Nat. Phys. **13**, 350 (2017).

[12] C.-K. Chan, N. H. Lindner, G. Refael, and P. A. Lee, Photocurrents in Weyl semimetals, Phys. Rev. B **95**, 041104(R) (2017).

[13] E. J. König, H.-Y. Xie, D. A. Pesin, and A. Levchenko, Photogalvanic effect in Weyl semimetals, Phys. Rev. B **96**, 075123 (2017).

[14] G. B. Osterhoudt, L. K. Diebel, M. J. Gray, X. Yang, J. Stanco, X. Huang, B. Shen, N. Ni, P. J. Moll, Y. Ran *et al.*, Colossal mid-infrared bulk photovoltaic effect in a type-I Weyl semimetal, Nat. Mater. **18**, 471 (2019).

[15] H. Yuan, X. Wang, B. Lian, H. Zhang, X. Fang, B. Shen, G. Xu, Y. Xu, S.-C. Zhang, H. Y. Hwang *et al.*, Generation and electric control of spin–valley-coupled circular photogalvanic current in WSe_2, Nat. Nanotechnol. **9**, 851 (2014).

[16] Q. Ma, S.-Y. Xu, C.-K. Chan, C.-L. Zhang, G. Chang, Y. Lin, W. Xie, T. Palacios, H. Lin, S. Jia *et al.*, Direct optical detection of Weyl fermion chirality in a topological semimetal, Nat. Phys. **13**, 842 (2017).

[17] Y. Gao, S. Kaushik, E. J. Philip, Z. Li, Y. Qin, Y. P. Liu, W. L. Zhang, Y. L. Su, X. Chen, H. Weng *et al.*, Chiral terahertz wave emission from the Weyl semimetal TaAs, Nat. Commun. **11**, 720 (2020).

[18] T. Morimoto and N. Nagaosa, Topological nature of nonlinear optical effects in solids, Sci. Adv. **2**, e1501524 (2016).

[19] J. Ahn, G.-Y. Guo, and N. Nagaosa, Low-frequency divergence and quantum geometry of the bulk photovoltaic effect in topological semimetals, Phys. Rev. X **10**, 041041 (2020).

[20] J. Ahn, G.-Y. Guo, N. Nagaosa, and A. Vishwanath, Riemannian geometry of resonant optical responses, Nat. Phys. **18**, 290 (2022).

[21] J. E. Sipe and A. I. Shkrebtii, Second-order optical response in semiconductors, Phys. Rev. B **61**, 5337 (2000).

[22] T. Holder, D. Kaplan, and B. Yan, Consequences of time-reversal-symmetry breaking in the light-matter interaction: Berry curvature, quantum metric, and diabatic motion, Phys. Rev. Res. **2**, 033100 (2020).

[23] N. Nagaosa and T. Morimoto, Concept of quantum geometry in optoelectronic processes in solids: application to solar cells, Adv. Mater. **29**, 1603345 (2017).

[24] R. von Baltz and W. Kraut, Theory of the bulk photovoltaic effect in pure crystals, Phys. Rev. B **23**, 5590 (1981).

[25] W. Kraut and R. von Baltz, Anomalous bulk photovoltaic effect in ferroelectrics: A quadratic response theory, Phys. Rev. B **19**, 1548 (1979).

[26] S. Chaudhary, C. Lewandowski, and G. Refael, Shift-current response as a probe of quantum geometry and electron-electron interactions in twisted bilayer graphene, Phys. Rev. Res. **4**, 013164 (2022).

[27] D. Kaplan, T. Holder, and B. Yan, Twisted photovoltaics at terahertz frequencies from momentum shift current, Phys. Rev. Res. **4**, 013209 (2022).

[28] Y. Gao, Y. Zhang, and D. Xiao, Tunable layer circular photogalvanic effect in twisted bilayers, Phys. Rev. Lett. **124**, 077401 (2020).

[29] A. Raj, S. Chaudhary, and G. A. Fiete, Photogalvanic response in multi-Weyl semimetals, Phys. Rev. Res. **6**, 013048 (2024).

[30] T. Xu, T. Morimoto, and J. E. Moore, Nonlinear optical effects in inversion-symmetry-breaking superconductors, Phys. Rev. B **100**, 220501(R) (2019).

[31] S. Nakamura, K. Katsumi, H. Terai, and R. Shimano, Nonreciprocal terahertz second-harmonic generation in superconducting NbN under supercurrent injection, Phys. Rev. Lett. **125**, 097004 (2020).

[32] H. Watanabe, A. Daido, and Y. Yanase, Nonreciprocal optical response in parity-breaking superconductors, Phys. Rev. B **105**, 024308 (2022).

[33] H. Tanaka, H. Watanabe, and Y. Yanase, Nonlinear optical responses in noncentrosymmetric superconductors, Phys. Rev. B **107**, 024513 (2023).

[34] M. Tinkham, Energy gap interpretation of experiments on infrared transmission through superconducting films, Phys. Rev. **104**, 845 (1956).

[35] L. H. Palmer and M. Tinkham, Far-infrared absorption in thin superconducting lead films, Phys. Rev. **165**, 588 (1968).

[36] J. Ahn and N. Nagaosa, Theory of optical responses in clean multi-band superconductors, Nat. Commun. **12**, 1617 (2021).

[37] M. Papaj and J. E. Moore, Current-enabled optical conductivity of superconductors, Phys. Rev. B **106**, L220504 (2022).

[38] L. Zhao, C. Belvin, R. Liang, D. Bonn, W. Hardy, N. Armitage, and D. Hsieh, A global inversion-symmetry-broken phase inside the pseudogap region of $YBa_2Cu_3O_y$, Nat. Phys. **13**, 250 (2017).

[39] L. P. Gor'kov and E. I. Rashba, Superconducting 2d system with lifted spin degeneracy: Mixed singlet-triplet state, Phys. Rev. Lett. **87**, 037004 (2001).

[40] E. Bauer and M. Sigrist, *Non-Centrosymmetric Superconductors: Introduction and Overview* (Springer, Berlin, Heidelberg, 2012), Vol. 847.

[41] S. Yip, Noncentrosymmetric superconductors, Annu. Rev. Condens. Matter Phys. **5**, 15 (2014).

[42] M. Smidman, M. Salamon, H. Yuan, and D. Agterberg, Superconductivity and spin–orbit coupling in non-centrosymmetric materials: a review, Rep. Prog. Phys. **80**, 036501 (2017).

[43] M. H. Fischer, M. Sigrist, D. F. Agterberg, and Y. Yanase, Superconductivity and local inversion-symmetry breaking, Annu. Rev. Condens. Matter Phys. **14**, 153 (2023).

[44] K. Nogaki and Y. Yanase, Even-odd parity transition in strongly correlated locally noncentrosymmetric superconductors: Application to $CeRh_2As_2$, Phys. Rev. B **106**, L100504 (2022).

[45] K. Sonowal, A. Parafilo, M. Boev, V. Kovalev, and I. Savenko, Second-harmonic generation in fluctuating Ising superconductors, 2D Mater. **10**, 045004 (2023).

[46] H. Watanabe, A. Daido, and Y. Yanase, Nonreciprocal meissner response in parity-mixed superconductors, Phys. Rev. B **105**, L100504 (2022).

[47] Y. Saito, Y. Nakamura, M. S. Bahramy, Y. Kohama, J. Ye, Y. Kasahara, Y. Nakagawa, M. Onga, M. Tokunaga, T. Nojima *et al.*, Superconductivity protected by spin–valley locking in ion-gated MoS_2, Nat. Phys. **12**, 144 (2016).

[48] P. Wan, O. Zheliuk, N. F. Q. Yuan, X. Peng, L. Zhang, M. Liang, U. Zeitler, S. Wiedmann, N. E. Hussey, T. T. M. Palstra *et al.*, Orbital Fulde–Ferrell–Larkin–Ovchinnikov state in an Ising superconductor, Nature (London) **619**, 46 (2023).

[49] X. Zhang, J. Liu, and F. Liu, Topological superconductivity based on antisymmetric spin–orbit coupling, Nano Lett. **22**, 9000 (2022).

[50] Z. S. Gao, X.-J. Gao, W.-Y. He, X. Y. Xu, T. K. Ng, and K. T. Law, Topological superconductivity in multifold fermion metals, Quantum Front. **1**, 3 (2022).

[51] Y. Yanase and M. Sigrist, Helical superconductivity in noncentrosymmetric superconductors with dominantly spin triplet pairing, J. Phys. Soc. Jpn. **77**, 342 (2008).

[52] Q. H. Wang, K. Kalantar-Zadeh, A. Kis, J. N. Coleman, and M. S. Strano, Electronics and optoelectronics of two-dimensional transition metal dichalcogenides, Nat. Nanotechnol. **7**, 699 (2012).

[53] S. Manzeli, D. Ovchinnikov, D. Pasquier, O. V. Yazyev, and A. Kis, 2D transition metal dichalcogenides, Nat. Rev. Mater. **2**, 17033 (2017).

[54] H. Yang, S. W. Kim, M. Chhowalla, and Y. H. Lee, Structural and quantum-state phase transitions in van der Waals layered materials, Nat. Phys. **13**, 931 (2017).

[55] A. H. Castro Neto, Charge density wave, superconductivity, and anomalous metallic behavior in 2D transition metal dichalcogenides, Phys. Rev. Lett. **86**, 4382 (2001).

[56] J. Lu, O. Zheliuk, I. Leermakers, N. F. Yuan, U. Zeitler, K. T. Law, and J. Ye, Evidence for two-dimensional Ising superconductivity in gated MoS_2, Science **350**, 1353 (2015).

[57] C.-X. Liu, Unconventional superconductivity in bilayer transition metal dichalcogenides, Phys. Rev. Lett. **118**, 087001 (2017).

[58] F. Zhang, W. Zheng, Y. Lu, L. Pabbi, K. Fujisawa, A. L. Elías, A. R. Binion, T. Granzier-Nakajima, T. Zhang, Y. Lei *et al.*, Superconductivity enhancement in phase-engineered molybdenum carbide/disulfide vertical heterostructures, Proc. Natl. Acad. Sci. USA **117**, 19685 (2020).

[59] C. Lane and J.-X. Zhu, Identifying topological superconductivity in two-dimensional transition-metal dichalcogenides, Phys. Rev. Mater. **6**, 094001 (2022).

[60] N. F. Q. Yuan, K. F. Mak, and K. T. Law, Possible topological superconducting phases of MoS_2, Phys. Rev. Lett. **113**, 097001 (2014).

[61] D. Möckli and M. Khodas, Robust parity-mixed superconductivity in disordered monolayer transition metal dichalcogenides, Phys. Rev. B **98**, 144518 (2018).

[62] Y. Yuan, J. Pan, X. Wang, Y. Fang, C. Song, L. Wang, K. He, X. Ma, H. Zhang, F. Huang *et al.*, Evidence of anisotropic majorana bound states in 2M-WS_2, Nat. Phys. **15**, 1046 (2019).

[63] A. K. Nayak, A. Steinbok, Y. Roet, J. Koo, G. Margalit, I. Feldman, A. Almoalem, A. Kanigel, G. A. Fiete, B. Yan *et al.*, Evidence of topological boundary modes with topological nodal-point superconductivity, Nat. Phys. **17**, 1413 (2021).

[64] R. Roldán, E. Cappelluti, and F. Guinea, Interactions and superconductivity in heavily doped MoS_2, Phys. Rev. B **88**, 054515 (2013).

[65] Y.-T. Hsu, A. Vaezi, M. H. Fischer, and E.-A. Kim, Topological superconductivity in monolayer transition metal dichalcogenides, Nat. Commun. **8**, 14985 (2017).

[66] S. C. De la Barrera, M. R. Sinko, D. P. Gopalan, N. Sivadas, K. L. Seyler, K. Watanabe, T. Taniguchi, A. W. Tsen, X. Xu, D. Xiao *et al.*, Tuning Ising superconductivity with layer and spin–orbit coupling in two-dimensional transition-metal dichalcogenides, Nat. Commun. **9**, 1427 (2018).

[67] Y. Li, H. Zheng, Y. Fang, D. Zhang, Y. Chen, C. Chen, A. Liang, W. Shi, D. Pei, L. Xu *et al.*, Observation of topological superconductivity in a stoichiometric transition metal dichalcogenide 2M-WS_2, Nat. Commun. **12**, 2874 (2021).

[68] R. Oiwa, Y. Yanagi, and H. Kusunose, Theory of superconductivity in hole-doped monolayer MoS_2, Phys. Rev. B **98**, 064509 (2018).

[69] X. Xi, Z. Wang, W. Zhao, J.-H. Park, K. T. Law, H. Berger, L. Forró, J. Shan, and K. F. Mak, Ising pairing in superconducting $NbSe_2$ atomic layers, Nat. Phys. **12**, 139 (2016).

[70] Y. Xing, K. Zhao, P. Shan, F. Zheng, Y. Zhang, H. Fu, Y. Liu, M. Tian, C. Xi, H. Liu *et al.*, Ising superconductivity

and quantum phase transition in macro-size monolayer $NbSe_2$, Nano Lett. **17**, 6802 (2017).

[71] Y. Yang, S. Fang, V. Fatemi, J. Ruhman, E. Navarro-Moratalla, K. Watanabe, T. Taniguchi, E. Kaxiras, and P. Jarillo-Herrero, Enhanced superconductivity upon weakening of charge density wave transport in $2H$-TaS_2 in the two-dimensional limit, Phys. Rev. B **98**, 035203 (2018).

[72] C.-S. Lian, C. Si, and W. Duan, Unveiling charge-density wave, superconductivity, and their competitive nature in two-dimensional $NbSe_2$, Nano Lett. **18**, 2924 (2018).

[73] C.-S. Lian, Interplay of charge ordering and superconductivity in two-dimensional $2H$ group V transition-metal dichalcogenides, Phys. Rev. B **107**, 045431 (2023).

[74] C.-S. Lian, C. Heil, X. Liu, C. Si, F. Giustino, and W. Duan, Intrinsic and doping-enhanced superconductivity in monolayer $1H$-TaS_2: Critical role of charge ordering and spin-orbit coupling, Phys. Rev. B **105**, L180505 (2022).

[75] D. Wickramaratne, S. Khmelevskyi, D. F. Agterberg, and I. I. Mazin, Ising superconductivity and magnetism in $NbSe_2$, Phys. Rev. X **10**, 041003 (2020).

[76] W. Chen, Q. Zhu, Y. Zhou, and J. An, Topological Ising pairing states in monolayer and trilayer TaS_2, Phys. Rev. B **100**, 054503 (2019).

[77] A. Hamill, B. Heischmidt, E. Sohn, D. Shaffer, K.-T. Tsai, X. Zhang, X. Xi, A. Suslov, H. Berger, L. Forró *et al.*, Two-fold symmetric superconductivity in few-layer $NbSe_2$, Nat. Phys. **17**, 949 (2021).

[78] V. Vaňo, S. C. Ganguli, M. Amini, L. Yan, M. Khosravian, G. Chen, S. Kezilebieke, J. L. Lado, and P. Liljeroth, Evidence of nodal superconductivity in monolayer 1H-TaS_2 with hidden order fluctuations, Adv. Mater. **35**, 2305409 (2023).

[79] W. Wan, P. Dreher, D. Muñoz-Segovia, R. Harsh, H. Guo, A. J. Martínez-Galera, F. Guinea, F. de Juan, and M. M. Ugeda, Observation of superconducting collective modes from competing pairing instabilities in single-layer $NbSe_2$, Adv. Mater. **34**, 2206078 (2022).

[80] S. Hörhold, J. Graf, M. Marganska, and M. Grifoni, Two-bands Ising superconductivity from Coulomb interactions in monolayer, 2D Mater. **10**, 025008 (2023).

[81] C.-W. Cho, J. Lyu, L. An, T. Han, K. T. Lo, C. Y. Ng, J. Hu, Y. Gao, G. Li, M. Huang, N. Wang, J. Schmalian, and R. Lortz, Nodal and nematic superconducting phases in $NbSe_2$ monolayers from competing superconducting channels, Phys. Rev. Lett. **129**, 087002 (2022).

[82] G. Margalit, E. Berg, and Y. Oreg, Theory of multi-orbital topological superconductivity in transition metal dichalcogenides, Ann. Phys. **435**, 168561 (2021).

[83] W.-Y. He, B. T. Zhou, J. J. He, N. F. Yuan, T. Zhang, and K. T. Law, Magnetic field driven nodal topological superconductivity in monolayer transition metal dichalcogenides, Commun. Phys. **1**, 40 (2018).

[84] D. Shaffer, J. Kang, F. J. Burnell, and R. M. Fernandes, Crystalline nodal topological superconductivity and Bogoliubov Fermi surfaces in monolayer $NbSe_2$, Phys. Rev. B **101**, 224503 (2020).

[85] Y. Bao, Y. Li, K. Xia, and L. Meng, Magnetic field regulation of nodal topological superconducting states in monolayer Ising superconductor $NbSe_2$, Phys. Status Solidi RRL **17**, 2300135 (2023).

[86] I. Silber, S. Mathimalar, I. Mangel, A. K. Nayak, O. Green, N. Avraham, H. Beidenkopf, I. Feldman, A. Kanigel, A. Klein *et al.*, Two-component nematic superconductivity in 4Hb-TaS_2, Nat. Commun. **15**, 824 (2024).

[87] J. A. Galvis, L. Chirolli, I. Guillamón, S. Vieira, E. Navarro-Moratalla, E. Coronado, H. Suderow, and F. Guinea, Zero-bias conductance peak in detached flakes of superconducting $2H$-TaS_2 probed by scanning tunneling spectroscopy, Phys. Rev. B **89**, 224512 (2014).

[88] E. Navarro-Moratalla, J. O. Island, S. Manas-Valero, E. Pinilla-Cienfuegos, A. Castellanos-Gomez, J. Quereda, G. Rubio-Bollinger, L. Chirolli, J. A. Silva-Guillén, N. Agraït *et al.*, Enhanced superconductivity in atomically thin TaS_2, Nat. Commun. **7**, 11043 (2016).

[89] P. Törmä, Essay: Where can quantum geometry lead us? Phys. Rev. Lett. **131**, 240001 (2023).

[90] S. A. Chen and K.T. Law, Ginzburg-Landau theory of flat-band superconductors with quantum metric, Phys. Rev. Lett. **132**, 026002 (2024).

[91] J.-X. Hu, S. A. Chen, and K. T. Law, Anomalous coherence length in superconductors with quantum metric, arXiv:2308.05686.

[92] A. Julku, T. J. Peltonen, L. Liang, T. T. Heikkilä, and P. Törmä, Superfluid weight and Berezinskii-Kosterlitz-Thouless transition temperature of twisted bilayer graphene, Phys. Rev. B **101**, 060505(R) (2020).

[93] J. Herzog-Arbeitman, V. Peri, F. Schindler, S. D. Huber, and B. A. Bernevig, Superfluid weight bounds from symmetry and quantum geometry in flat bands, Phys. Rev. Lett. **128**, 087002 (2022).

[94] F. Xie, Z. Song, B. Lian, and B. A. Bernevig, Topology-bounded superfluid weight in twisted bilayer graphene, Phys. Rev. Lett. **124**, 167002 (2020).

[95] N. Verma, T. Hazra, and M. Randeria, Optical spectral weight, phase stiffness, and T_c bounds for trivial and topological flat band superconductors, Proc. Natl. Acad. Sci. USA **118**, e2106744118 (2021).

[96] G. E. Topp, C. J. Eckhardt, D. M. Kennes, M. A. Sentef, and P. Törmä, Light-matter coupling and quantum geometry in moiré materials, Phys. Rev. B **104**, 064306 (2021).

[97] X.-L. Qi, T. L. Hughes, and S.-C. Zhang, Topological invariants for the Fermi surface of a time-reversal-invariant superconductor, Phys. Rev. B **81**, 134508 (2010).

[98] M. Sato, Nodal structure of superconductors with time-reversal invariance and Z_2 topological number, Phys. Rev. B **73**, 214502 (2006).

[99] E. Berg, C.-C. Chen, and S. A. Kivelson, Stability of nodal quasiparticles in superconductors with coexisting orders, Phys. Rev. Lett. **100**, 027003 (2008).

[100] B. Béri, Topologically stable gapless phases of time-reversal-invariant superconductors, Phys. Rev. B **81**, 134515 (2010).

[101] A. Ribak, R. M. Skiff, M. Mograbi, P. Rout, M. Fischer, J. Ruhman, K. Chashka, Y. Dagan, and A. Kanigel, Chiral superconductivity in the alternate stacking compound 4Hb-TaS_2, Sci. Adv. **6**, eaax9480 (2020).

[102] R. Seshadri, M. Khodas, and D. Meidan, Josephson junctions of topological nodal superconductors, SciPost Phys. **12**, 197 (2022).